Accepted Manuscript

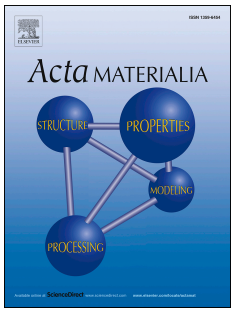

Simulation and experimental study of the particle size distribution and pore effect on the crystallization of glass powders

Roger G. Fernandes, Raphael M.C.V. Reis, Raúl R. Tobar, Edgar D. Zanotto, Eduardo B. Ferreira

PII: S1359-6454(19)30333-7

DOI: https://doi.org/10.1016/j.actamat.2019.05.049

Reference: AM 15321

To appear in: *Acta Materialia*

Received Date: 18 March 2019

Revised Date: 16 May 2019

Accepted Date: 23 May 2019

Please cite this article as: R.G. Fernandes, R.M.C.V. Reis, R.R. Tobar, E.D. Zanotto, E.B. Ferreira, Simulation and experimental study of the particle size distribution and pore effect on the crystallization of glass powders, *Acta Materialia*, https://doi.org/10.1016/j.actamat.2019.05.049.

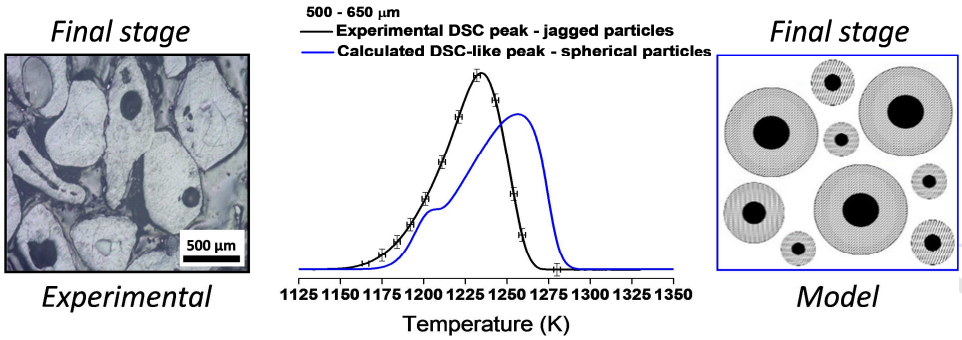

Simulation and experimental study of the particle size distribution and pore effect on the crystallization of glass powders

Roger G. Fernandes[1], Raphael M. C. V. Reis[2], Raúl R. Tobar[1], Edgar D. Zanotto[3], Eduardo B. Ferreira[1]

[1] Department of Materials Engineering, Engineering School of São Carlos, University of São Paulo, USP, 400 Trabalhador São-carlense Avenue, São Carlos-SP, Brazil, Zip code 13566-590

[2] Department of Metallurgical and Materials Engineering, Fluminense Federal University, UFF, 420 dos Trabalhadores Avenue, Volta Redonda-RJ, Brazil, Zip code 27255-125

[3] Vitreous Materials Laboratory, Department of Materials Engineering, Federal University of São Carlos, UFSCar, Washington Luis Road, Km 235, São Carlos-SP, Brazil, Zip code 13565-905

Abstract

Surface nucleation is a frequent phenomenon and plays an essential role in the crystallization of most glasses, especially glass powders used in sintered glass-ceramics, for example. A technique often employed to study the crystallization kinetics of glassy powders is Differential Scanning Calorimetry (DSC). However, the shape of the crystallization peak profile is usually very complex. For instance, in certain cases of surface nucleation, the crystal growth dimensionality may change during crystallization after crystal impingement, and a large density difference between the parent glass and the resulting crystalline phases may produce cavitation pores in the particle volume. Finally, crushed glass particles are not regularly shaped, as assumed in most models. Hence, to evaluate the crystallization kinetics of glass powders by DSC experiments, in this work, we modified and tested a particle

crystallization model using the DSC crystallization peaks of jagged powders of a non-stoichiometric diopside ($0.9\mathrm{CaO}.\ 0.7\mathrm{MgO}.\ 2\mathrm{SiO_2}$) glass having different granulometries and a large crystal/glass density difference. The *Reis-Zanotto* model was adapted to include two complex variables: particle size distribution and crystallization-induced porosity. As predicted by the modified model, we confirmed the radical change of the DSC peak shape for some particle sizes as a result of crystal impingement and pore formation. This combined experimental-simulation study demonstrates that the adapted model can describe this type of complex and yet frequent crystallization case.

Keywords: Kinetics; Crystallization; Non-metallic glasses (silicates); Differential Scanning Calorimetric (DSC); Size effect; Spherical particles

1. Introduction

Diopside ($CaO.MgO.2SiO_2$) has been used as a basis for glass compositions to develop sintered glass-ceramics having unique thermal [1], corrosion [2] and dielectric [3] properties and high fracture strength [4], which combined with low sintering temperature [5] make them attractive for several applications. Bioactive [6] and dental materials [7], marble-like tiles for architecture and construction [8], and substrates for electronic devices [3-5] are some examples. Also, because of its low dielectric constant and loss in the microwave range, along with a low firing temperature suitable for metallic conductors, diopside is also being used for LTCC (Low-Temperature Co-fired Ceramics) in the production of substrates for electronic circuits for communications systems.

Diopside-based glasses sinter by viscous flow with concurrent surface crystallization. The glass particle size and shape affect the sintering and crystallization kinetics, resulting in

crystalline grains and pores of different morphologies and proportions in the microstructure, whose control allows a design for specific purposes [8-11]. For instance, small jagged particles sinter faster than coarse spherical particles. The careful control of densification and crystallization kinetics yields sintered products with optimal properties. There are different models for the crystallization kinetics of glass particles, which are presented in the next section.

In the case of diopside, an extra complexity arises regarding the density of the crystalline phase (3.29 g/cm^3), which is considerably higher than that of glass (2.84 g/cm^3) of the same composition [12]. Thus, for diopside glass particles, the increase of the crystallized surface layer thickness gives rise to hydrostatic tensile stresses in the confined residual glass that decay by the formation of a single pore within the interior of each particle [12,13].

The objective of this work was to propose and test a modified model able to describe the complex crystallization case of an ensemble of near-stoichiometric diopside glass particles. For this task, we **extended the *Reis-Zanotto* (RZ)** [14] **model** for particle crystallization kinetics to include **particle size distribution** and **crystallization-induced porosity.** We used this particular glass having these two complicating (but frequent found) features and characterized its crystallization behavior by Differential Scanning Calorimetry (DSC). Finally, we compared the results with DSC-like crystallization peaks calculated using the adapted model. The model modifications and tests are thoroughly described in the section that follows.

2. Theory

The classical model of Johnson & Mehl [15], Avrami [16-18], and Kolmogorov [19] (JMAK) forms the theoretical basis for understanding the overall crystallization kinetics of glasses by nucleation and growth [20,21], from which the isothermal time-transformed fraction $\alpha(t)$ is given by

$$\alpha(t) = 1 - \exp(-\alpha'(t)), \qquad (1)$$

where $\alpha'(t)$ is the ratio V/V_o or S/S_o between the volume or surface of the growing crystals and their initial values, disregarding their overlap, also known as extended volume. $\alpha'(t)$ can reach values > 1, whereas $\alpha(t) \leq 1$.

Crystallization of glass particle compacts, a common case in engineering applications, such as ceramic-tile glazes and sintered glass-ceramics, is a more complex, special case of transformation kinetics since small particles do not satisfy the infinite volume and surface constraints considered in the JMAK approach [22]. However, several analytical models [7,23-25] use the JMAK theory to calculate the crystallization kinetics of glass particles. Authors such as Müller (1989) [26], Weinberg (1991) [27] and Villa & Rios (2010) [28] used other approaches, however, their models are mathematically complex and relatively difficult to apply, even though the approaches developed by Weinberg and Villa & Rios provide exact solutions to the problem.

Recently, Reis and Zanotto [14] proposed a new model for the non-isothermal crystallization kinetics of spherical particles, $\alpha_V(T)$, with a finite number of heterogeneous nuclei randomly distributed on the particle surface. Their model, Eq. (2), combines the JMAK expression for the crystallized surface fraction, $\alpha_S(T)$, and the volumetric crystallized fraction related to the inward growth of a continuous crystalline layer from the surface of a

particle, $\alpha_{layer}(T)$. The model may also consider the crystallization from internal nucleation sites.

$$\alpha_V(T) = \alpha_S(T) \cdot \alpha_{layer}(T) \tag{2}$$

$\alpha_{\text{layer}}(\text{T})$ is the thickness of a continuous crystallized layer from the particle surface, i.e., considering a very large N_s. However, due to the finite number of nucleation sites, only a fraction of the particle surface crystallizes in the initial stages; therefore $\alpha_{\text{S}}(\text{T}) \leq 1$. The product $\alpha_{\text{S}}(\text{T}) \cdot \alpha_{\text{layer}}(\text{T})$ in Eq. (2) accounts for this incomplete transformation of the layer in the beginning.

For a spherical particle, $\alpha_{layer}(T)$ is given by the classic result known as volume contraction model or Jander equation [29], Eq. (3),

$$\alpha_{layer}(T) = 1 - \left(1 - \frac{h(T)}{R}\right)^3, \tag{3}$$

where R is the particle radius and $h(T)$ is the thickness of the surface layer formed by crystals that nucleate at the particle surface and grow inwards. If the crystalline and glassy phases have the same density, Eq. (4) is valid for $h(T) \leq R$, *i.e.*, until the crystalline layer reaches the particle center. Considering heating at a constant rate q,

$$h(T) = \int_{T_0}^{T} \frac{U(T)}{q}\, dT, \tag{4}$$

where T_0 is the initial temperature, which is set to a temperature in which the crystal growth rate is insignificant, and $U(T)$ is the crystal growth rate in the interval between T_0 and the final temperature of study, T.

For particles with a relatively large number of surface nuclei, the crystals cover the surface ($\alpha_S \sim 1$) before reaching the particle center. From this moment on, the crystallization kinetics

is described only by the increase of the surface layer thickness. This change in transformation dimensionality, from 3D to 1D, can be detected as shoulder in DSC crystallization peaks [26].

2.1. Surface crystallization kinetics of square crystals

The crystallization of our diopside glass particles starts at their surfaces from a fixed concentration of nuclei, N_s (sites/m^2). The diopside crystals are nearly square; therefore, we may use the JMAK expression for square crystals to estimate the surface crystallized fraction in a non-isothermal regime, considering that the square diagonal is the direction of the fastest crystal growth, and thus it is equal to $2.h(T)$.

$$\alpha_S(T) = 1 - \exp\left(-2.N_s.\left(\int_{T_0}^{T} \frac{U(T)}{q} dT\right)^2\right). \quad (5)$$

2.2. Crystallization-induced porosity

To estimate the effect of pore formation on the crystallization kinetics, we assume that surface crystallization fixes the particle volume at the beginning of phase transformation–as soon as a rigid crystalline crust forms on the particle surface–and that pores nucleate in the particle center and grow radially, simultaneously with the crystallized surface layer (Figure 1), until they meet. We will refer to these pores as “density pores.” Therefore, the crystallization front never reaches the particle center. Instead, it stops abruptly at the crystal-pore interface, causing a sudden end of the DSC crystallization peak.

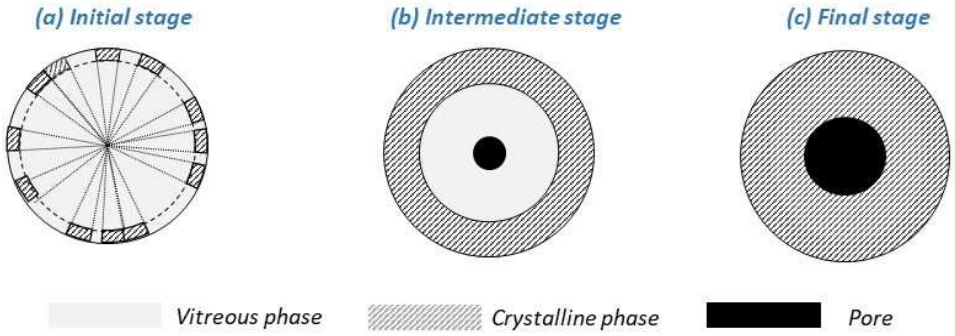

Figure 1. Schematics of different stages of spherical-particle crystallization: (a) crystallization starts from a finite number of surface nuclei; (b) after crystal impingement crystallization proceeds by decreasing the residual glass volume simultaneously with the nucleation and expansion of a central pore; and finally (c) crystallization ends at the pore interface.

For spherical particles, each nucleated pore grows up to a maximum volume given by

$$V_P^{max} = V_0\left(1 - \frac{\rho_g}{\rho_c}\right), \tag{6}$$

where V_0 is the initial particle volume, and ρ_C and ρ_G are the crystal and glass densities, respectively. When $\rho_g = \rho_c$, there is no stress in the residual glass, and a pore is not formed, *i.e.*, $V_p = 0$. Considering the maximum volumetric pore fraction $\alpha_P^{max} = \frac{V_P^{max}}{V_0}$, the maximum crystal volume fraction is given by $\alpha_C^{max} = 1 - \alpha_P^{max}$, and one can deduce that $\alpha_C^{max} = \frac{\rho_g}{\rho_c}$. In this case, the maximum layer thickness is

$$h^{max} = R \cdot \left(1 - \left(1 - \frac{\rho_c}{\rho_g}\right)^{1/3}\right). \tag{7}$$

This is reached when the crystallization front reaches the pore. For diopside crystal [12], $\rho_c = 3.29\ g/cm^3$. The density of the glass used in this work is $\rho_g = 2.87\ g/cm^3$, measured by He pycnometry, as subsequently detailed. Thus, $\alpha_C^{max} = 0.87$ and $h^{max} \cong 0.50R$. The

difference between glass and crystal densities limits the maximum crystallized volume fraction to the initial particle volume.

The crystallized mass fraction $X(T)$ can then be calculated for an ensemble of spherical particles of the same R, considering the effect of a finite number of nucleation sites as

$$X(T) = \alpha_V(T)\frac{\rho_c}{\rho_g}, \tag{8}$$

with $0 \leq X(T) \leq 1$.

2.3. Particle size distribution

The *Reis-Zanotto* model can be extended for a particle size distribution by considering the weighted contribution of each particle size interval i. Thus, the crystallized fraction is given by the average crystallized fraction weighted by the volume fraction of particles at each size interval v_i, Eq. (9).

$$X(T) = \sum_{i=1}^{n} X_i(T) \cdot v_i. \tag{9}$$

2.4. DSC crystallization peak

The intensity of a DSC crystallization peak is proportional to the rate of heat released by the sample during phase transformation. The area under the DSC crystallization peak of partially crystallized glass particles may then be associated with the mass of residual glass in the sample [30]. Hence, the crystallized mass fraction given by Eq. (9) may be directly related to the corresponding DSC crystallization peak. Considering a normalized peak with unit area, i.e., with 100% of its mass transformed, the $DSC(T)$ signal can be defined as

$$DSC(T) = \frac{dX(T)}{dT}. \quad (10)$$

3. Materials and Methods

A glass with composition $0.95\mathrm{CaO}.0.73\mathrm{MgO}.2\mathrm{SiO_2}$, close but off the stoichiometric diopside ($CaO.MgO.2SiO_2$), was prepared from reagent grade raw materials (SiO_2, $CaCO_3$, MgO). The strategy was to study a relatively more complex, non-stoichiometric case–yet not too far from the stoichiometry-which is often encountered in real applications to make sure that crystalline diopside would crystallize and induce density pores.

A batch for 200 g glass was weighed, homogenized in a high-impact mill Pulverisette 6 (Fritsch, Germany) and melted in a platinum crucible in a bottom-load electric furnace at 1773 K for 4 h. Glass samples were obtained by splat-cooling the melt between stainless steel plates. The glass composition was analyzed by X-ray fluorescence (XRF) in a sequential X-ray Fluorescence Spectrometer S8 Tiger (Bruker, Germany). The quantitative elemental analysis was performed for a sample dissolved in molten lithium tetraborate and quenched into a glass. We made use of a calibration standard based on the following compounds: SiO_2, Al_2O_3, Fe_2O_3, MnO, MgO, CaO, Na_2O, K_2O, TiO_2, and P_2O_5. The density of a coarsely fragmented sample was determined by He pycnometry in an Ultrapyc 1220e (Quantachrome Instruments, USA).

The glass was hand-milled in an agate mortar with pestle. Samples of jagged particles of different granulometries were obtained by sieving through monofilament nylon meshes in the nominal granulometry ranges (µm): < 7, 7-20, 20-45, 45-76, 76-150, 150-300, 300-430, 430-500, 500-650, 650-800, 800-1000 and 1000-1500. The particle size distribution of samples passing through meshes with granulometry below 20 µm was determined by

dynamic image analysis in a Camsizer L (Retsch Technology, Germany) granulometer in dry mode. The high-speed image capture generated a fast and statistically reliable measure. The granulometry of particles passing through < 20-µm opening meshes was determined by low-angle light scattering in a Mastersize S (Malvern, UK) granulometer in wet mode. The powder samples were dispersed in deionized water by ultrasound. The Cansizer L and Mastersize S granulometers provide the equivalent circle and spherical diameter, respectively, as measures of particle size.

Differential Scanning Calorimetry (DSC) experiments were performed in a DSC 404 F1 Pegasus (Netzsch, Germany) at 10 K/min from 373 to 1763 K in air, with Pt pans and lids, sample mass of 50 mg and one empty lidded Pt pan as a reference. To prevent the crucible from sticking to the sample holder at high temperatures, we used an alumina 200-µm-thick disk below each pan. The temperature was calibrated by the average of three measurements of phase-transformation characteristic temperatures for the compounds: C_6H_5COOH (122.4 K), Ag_2SO_4 (699 K), CsCl (749 K) and $BaCO_3$ (1081 K). DSC was performed three times for each particle size.

The crystal phases appearing just after each DSC crystallization peak were characterized by X-ray Diffraction (XRD) in samples with extreme granulometries, < 7 µm and 430-500 µm, using a D5005 X-ray diffractometer (Siemens, Germany) at 40 mA, 40 kV, with CuKα (1.5406 Å) X-ray radiation. The XRD samples were prepared by die-pressing the glass powders at 104 MPa and submitting the obtained disk-shaped compacts to non-isothermal heat treatments (10 K/min) in the DSC furnace. We also performed DSC on cooling to search for any reversible transformation. The maximum temperatures 1323, 1503 and 1553 K were somewhat above the endpoint of each crystallization peak (presented in the Results

Section), after which the DSC furnace was cooled down to room temperature at 40 K/min. The obtained patterns were indexed by comparison with JCPDS files [31].

We experimentally determined the crystal growth rates in this non-stoichiometric glass to use them for the DSC peak profile calculations. Two $U(T)$ values were obtained as the angular coefficient of straight lines fit to the crystallized surface layer thickness *versus* treatment time data points measured from samples isothermally treated at 1123 K for periods of 30, 60 and 180 min, and at 1150 K for periods of 30, 60 and 90 min. We also used a recently proposed method that enabled us to determine $U(T)$ between 1170 and 1275 K by performing a single DSC run [32], from which we obtained $U(T)$ by fitting a third-degree polynomial to the experimental data.

DSC-like crystallization curves were calculated using the Eqs. (8-10) for samples with granulometry higher than 20 μm. To test for the effect of the real particle size distribution (PSD), we made calculations using the measured PSD for each granulometry range as well as their average particle size (D_{50}). We used the growth rate curve fitted to the obtained measurements to our glass and, for comparison, we also used a $U(T)$ function fitted to data of several authors (compiled by Reinsch et al. [33]) in a wide temperature range, considering the screw-dislocation mechanism of crystal growth. The heating rate of 10 K/min used in the experiments was also used to calculate the DSC-like crystallization curves. We used a value of 10^{10} m^{-2} for N_S, determined from the best fit of the impingement temperature of surface crystals (Section 5.2).

The calculated DSC-like curves were compared to experimental crystallization peaks. To obtain a unit area and enable the comparison with the calculated peaks, the DSC crystallization peaks were normalized by dividing the corresponding DSC experimental data

points by the value of the total area under the peak, resulting in (K^{-1}) units. We considered a sigmoidal baseline, since the heat capacity changes with crystallization.

4. Results

4.1. Glass composition and particle size distribution of powders

The composition of the glass used in this work is 14.3 MgO, 25.9 CaO and 58.4 SiO_2 (wt%). Table S1 (Supplementary Materials) compares the stoichiometric diopside with the chemical composition of the glass used here and by other authors. Figure 2 shows the particle size distribution of the samples. The granulometric distributions are approximately unimodal, and for most size intervals the average value is greater than the upper opening size (diagonal of a square opening) of the corresponding sieve. This is because these jagged particles can pass through the sieve openings with their longest axis perpendicular to the sieve plane, leading to the observed larger equivalent-circle diameters. The characteristic granulometry parameters including the intercepts at 10, 50 and 90% (D_{10}, $D_{50,}$ and D_{90}) are summarized in the Supplementary Materials, Table S2.

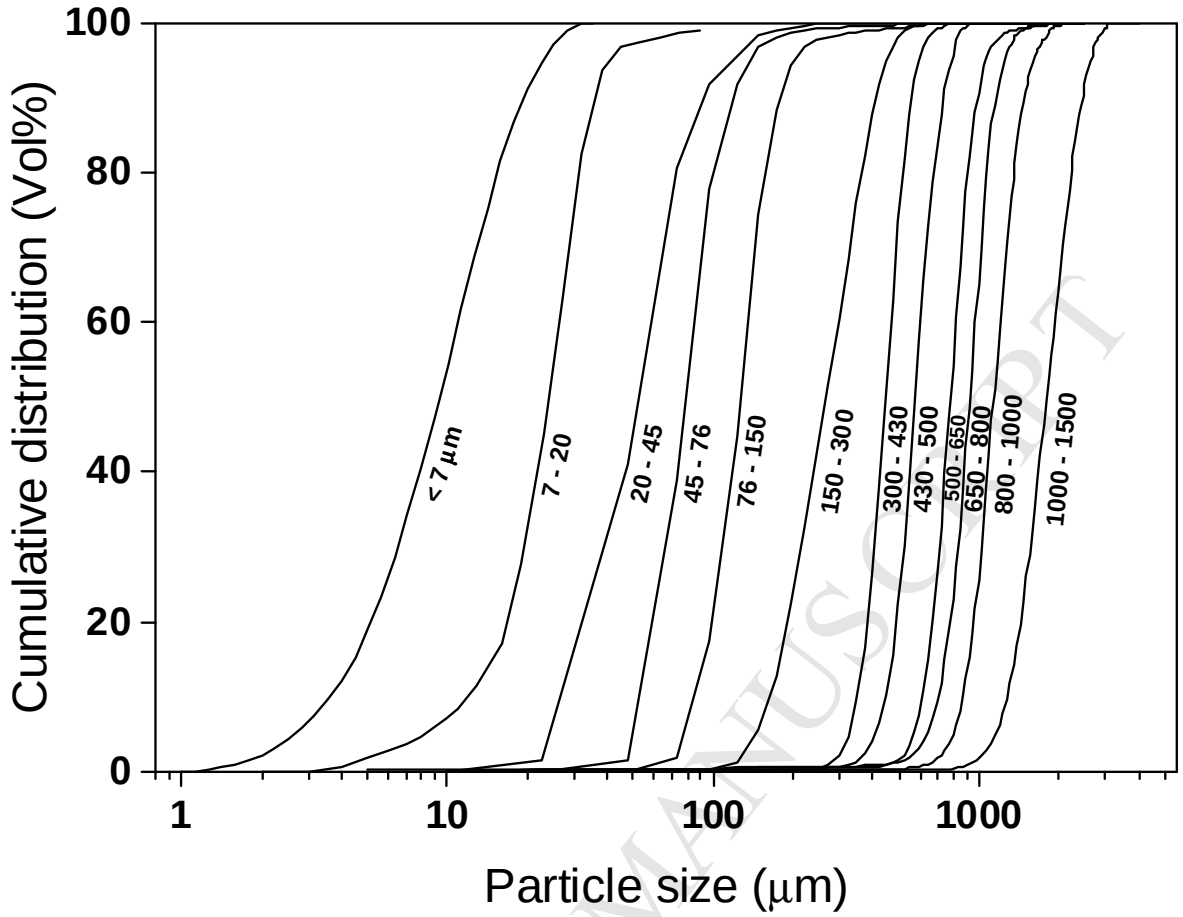

Figure 2. Particle size distributions of the jagged powdered glasses used here. The indicated values are the nominal lower and upper sizes (diagonal of a square opening) of the corresponding sieve, in micron (μm). The intercepts at 10, 50 and 90% (D_{10}, D_{50}, and D_{90}) of the cumulative size distributions are given in Table S2 of Supplementary Materials.

4.2. Differential Scanning Calorimetry of glass powders

The DSC traces of samples with different granulometries are shown in Figure 3. All the curves display the same general trend. The first baseline deviation refers to the glass transition, immediately followed by an endothermic peak, which can be attributed to a fictive temperature change, which results from using a heating rate in the DSC run that is different from the cooling rate used to produce the original glass[34]. The subsequent three

exothermic peaks refer to crystallization, from the most to the least intense at higher temperatures. Finally, two endothermic peaks arise with the melting of the previously crystallized phases. T_x, T_{imp}, $T_{p,}$ and T_l are the temperatures of crystallization onset, surface crystal impingement, crystallization peak maximum and the liquidus temperature, respectively. T_{imp} is determined at the inflection point after the shoulder at the low-temperature side of the first crystallization peak.

The average glass transition temperature (T_g) was $996\ K$ and did not show any significant change as a function of particle size, as expected. The glass transition temperature was determined at the intersection of extrapolated lines from the previous baseline and the low-temperature side of the neighbor endothermic peak. Both the average T_{x1} and T_{p1} shift approximately $56\ \mathrm{K}$ and $90\ \mathrm{K}$, respectively, to higher temperatures as the grain size increases. Table S2 and Figure S1 (Supplementary Materials) summarizes the characteristic temperatures for the different particle sizes, except for $T_{p3} = 1535\ K$ and $T_l = 1643\ K$, which are not affected by the particle size in the granulometric interval 20-1500 µm. For the 7-20 µm and < 7 µm samples, the third crystallization peak shifts to lower temperatures and almost vanishes.

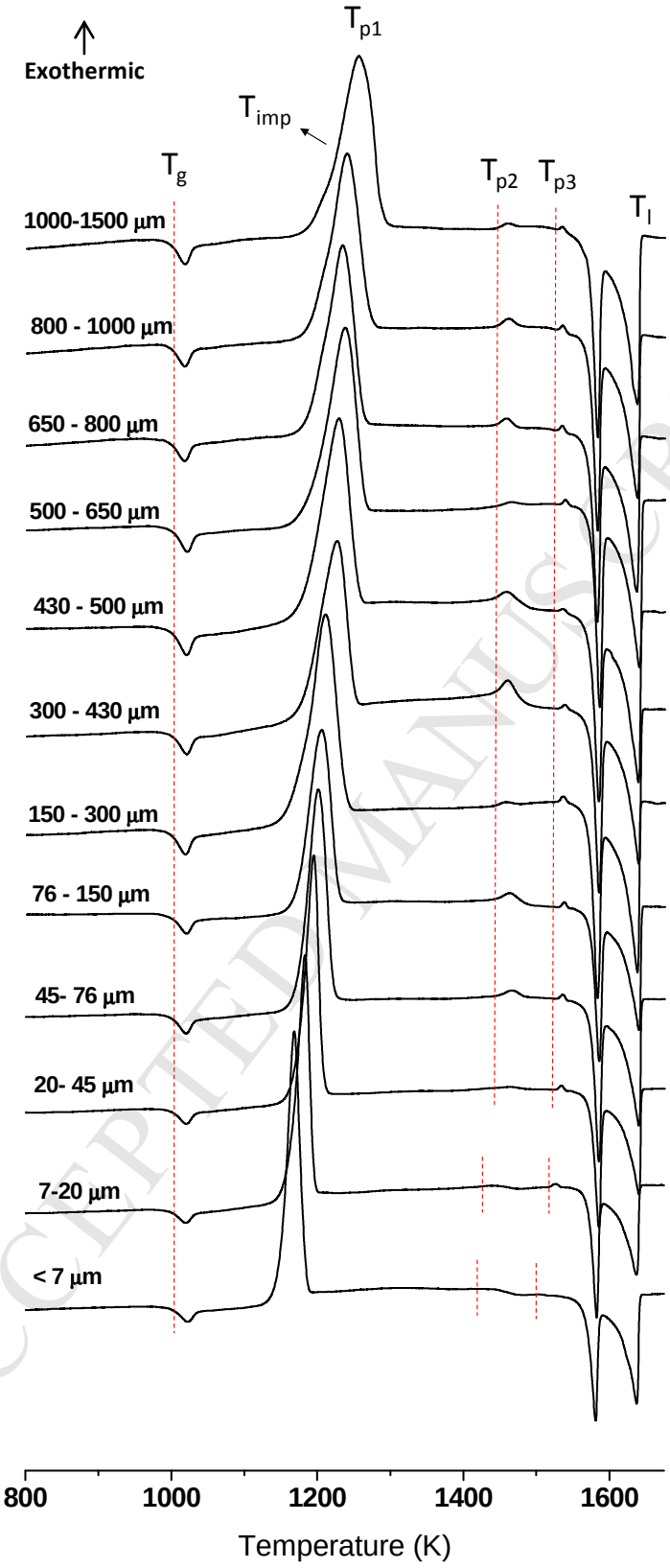

Figure 3. DSC traces at a heating rate of 10 K/min for glass samples with different granulometries. The dashed lines are a guide to the eye.

4.3. X-ray diffraction characterization of heat-treated powder compacts

Figure 4 shows the corresponding X-ray diffractograms of the samples with granulometries of < 7 μm and 430-500 μm, non-isothermally treated in the DSC furnace at the maximum temperatures of 1323, 1503 and 1553 K. We did not observe any transformation in the cooling of the samples inside the DSC furnace, indicating that no reversible transformation occurred (curves not shown for simplicity).

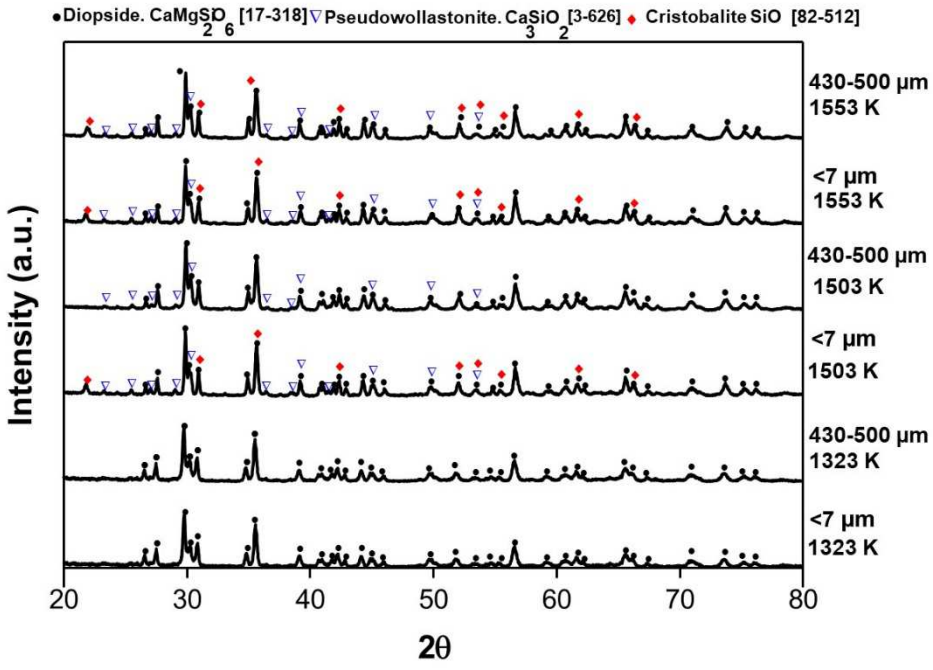

Figure 4. X-ray diffractograms of diopside glass compacts of granulometries below 7 μm and 430-500 μm, non-isothermally heated up to 1323, 1503 and 1553 K. The numbers in brackets correspond to the respective Powder Diffraction File, Inorganic Phases [31].

4.4. Diopside crystal growth rates

In the relatively narrow temperature range used here, $U(T)$ was obtained by fitting a third-degree polynomial expression to the experimental data ($\log(U[\mu m/min]) = a + bT +$

$cT^2 + dT^3$), for which the coefficients are $a = -387.89556$, $b = 0.82405\ K^{-1}$, $c = -5.80981 * 10^{-4} K^{-2}$, and $d = 1.36759 * 10^{-7} K^{-3}$. The temperature range of the measurements is well above the Stokes-Einstein breakdown temperature, T_b (for diopside, $T_b \sim 1100\ K$), where the crystal growth is driven by viscous flow[35,36]. The detailed crystal growth kinetics for this non-stoichiometric diopside glass will be reported elsewhere.

5. Discussion

5.1. Crystallization kinetics and phase formation

The chemical composition of our glass has a larger content of SiO_2 and a smaller amount of MgO than that of stoichiometric diopside (Table S1), and belongs to the compatibility triangle formed by $CaO.MgO.2SiO_2$ (diopside), SiO_2 and $CaO.SiO_2$ (pseudowollastonite) in the $CaO\text{-}MgO\text{-}SiO_2$ phase equilibrium diagram (PED) [37][36] (not shown). These are indeed the compositions of the detected phases after full crystallization. The *liquidus* estimated from the phase diagram, approximately $1633\ \mathrm{K}$, is very close to the melting endpoint temperature in the non-isothermal DSC curve ($T_l = 1643\ \mathrm{K}$). An even lower *liquidus* determined by DSC could be expected when the effect of a non-isothermal run is considered [38].

We observe in Figure 3 three exothermic peaks and two partially overlapped endothermic melting peaks. The combined analysis of the DSC and XRD results (Figures 3 and 4) for the samples with granulometries of <7 µm and 430-500 µm indicate that the three exothermic DSC peaks are due to the crystallization of diopside (D), pseudo-wollastonite (PW) and cristobalite (C), respectively. At $1323\ \mathrm{K}$ (after the first peak), only diopside crystals are detected by XRD for both samples. Further heating led to the crystallization of PW and C.

The 430-500-µm samples heat-treated above the second and third DSC crystallization peaks showed PW and C, respectively. For the samples with granulometry <7 µm, cristobalite had already been detected when the sample was treated up to $1503\ \mathrm{K}$. This is consistent with the shift of the third exothermic DSC peak for this particle size, probably because of the existence of finer regions of residual supercooled liquid between diopside crystals.

As the grain size increases, a shift of the first crystallization peak to higher temperatures is expected, since crystals growing from the surface can reach the center of smaller particles faster than in larger particles. The powder packing in the DSC pan may also affect T_{x1} and T_{p1}.

Differently from our results, only two crystallization peaks were observed by Fokin *et al.* [12], Reis [32,39] and Cassar [35] in samples of stoichiometric diopside glasses with irregular monolithic or plate shapes, or as a powder. On the other hand, Nascimento [40] observed only one crystallization peak for a glass with a non-stoichiometric composition similar to that used in this work. However, these authors have not presented DSC curves for a temperature as high as that of the third crystallization peak detected in this work, nor the melting region. They have also assigned two phases to the first DSC crystallization peak, showing that a wollastonite solid solution with diopside composition (or wollastonite-SS) crystallizes in the stressed residual glass (as the density of the crystallized diopside surface is substantially higher than that of the glass of the same composition). The second peak was then related to the polymorphic transformation of wollastonite-SS into diopside at higher temperatures. The characteristic temperatures of the crystallization peaks for our powders are shown in Table S3 (Supplementary Materials).

By XRD, we only observed the crystalline diopside related to the first DSC crystallization peak and no second phase relative to wollastonite-SS reported in the literature [12,35,39], probably because of the difference between the glass compositions (Table S1). In this paper, the glass density was experimentally measured, resulting in $\rho_g = 2.87\ g/cm^3$, while the density of the crystalline diopside, $\rho_c = 3.29\ g/cm^3$, was obtained in the literature [12].

5.2. Impingement of surface crystals and dimensionality change of crystallization

Figure 5a shows a magnification of the first DSC crystallization peak of samples with different granulometries. The maximum temperature of such peak shifts to higher temperatures, and it becomes wider and less intense as the particle size increases. For the samples with granulometries of 150-300 to 1000-1500 µm, a shoulder–easily visualized in the first derivative curves–appears before the maximum, as shown in Figure 5b. Figure 5c shows in detail the first DSC crystallization peak for the 800-1000-µm sample together with its corresponding first derivative, where it is possible to see the shoulder at the low-temperature side of the peak.

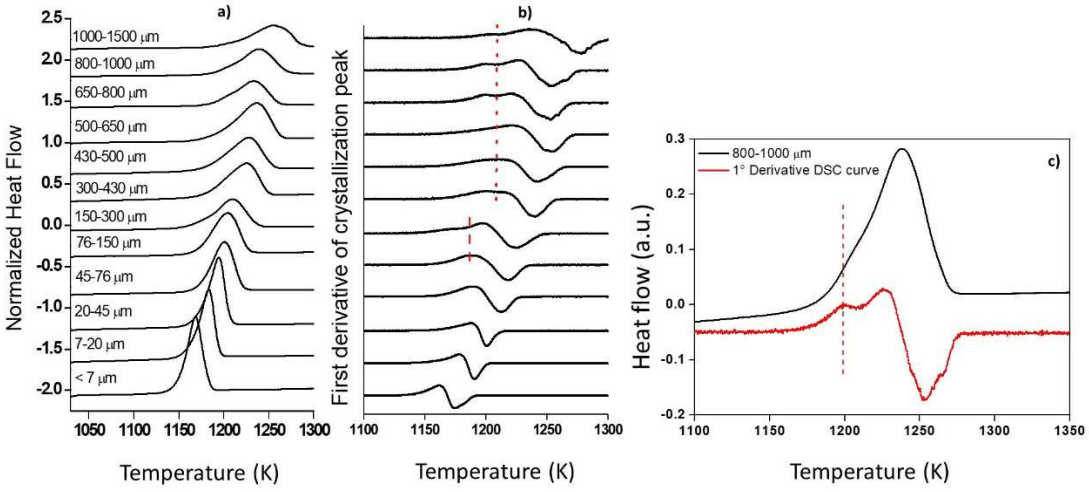

Figure 5. a) First (low temperature) DSC crystallization peak of diopside glass powders with different granulometries at a heating rate of 10 K/min; b) first derivatives of the first crystallization peaks; and c) magnification of the first crystallization peak and its first derivative for the 800-1000-µm sample. The dashed lines in b) and c) indicate the impingement temperature (T_{imp}).

To the best of our knowledge, Müller [26] was the first to observe that the shoulder in the DSC crystallization peak of glass powders changes with sample granulometry. He attributed this phenomenon to the change in the crystallization mode (from 3D to 1D), in that case, for a cordierite glass showing heterogeneous crystallization, similar to the diopside glass of this work. This shoulder was also observed in stoichiometric diopside glasses by some of us [32]. For relatively small particles, the transformation from the surface confounds with volume crystallization. Consequently, only a sharp DSC crystallization peak can be seen. As the particle size increases, an impingement occurs before reaching the whole transformation peak, and the 3D stage of the crystallization peak becomes more and more insignificant as the surface-to-volume ratio decreases.

We may define an impingement temperature, T_{imp}, and relate it to an inflection point in the first DSC crystallization peak, detected here as the first peak in the 1st derivative curve. The dashed vertical line in Figure 5b shows that T_{imp} occurs at the same temperature (1198 K) for samples with granulometries > 300 µm, and at $1175\ K$ for 150-300-µm; for samples with granulometries < 150 µm, it is not clearly shown.

T_{imp} must be the same for samples with the same surface density of nucleation sites (N_s). This was observed for samples with granulometries > 300 µm. However, N_s is very sensitive to surface processing [41]. The smaller the granulometry, the higher the chance of mechanical damage on the surface of the particles during the comminution process, which in turn increases N_s and decreases the period crystals grow on the surface to meet their neighboors. The earlier the surface crystals impinge, the lower the T_{imp}, as observed for the particle distributions below 150-300 µm. As the average particle size decreases, the sintering ability tends to increase as a result of a higher surface-to-volume ratio. Consequently, the contribution of the 3D crystallization mode at the left of the DSC crystallization peak becomes more important.

The RZ model, extended here to include the particle size and pore effect was able to predict the shoulder reported by Müller [26] in the DSC crystallization peaks when complete crystal impingement at the particle surface takes place. Independently of the particle size, the shoulders occurred at the same temperature ($1198\ K$), indicating a similar value of N_s for all the samples. As expected, the DSC intensity at the shoulder temperature increases as the particle size decreases. For large particles, the crystallized surface layer at the stage crystals meet on the surface is insignificant compared with the residual glass volume. Hence, there is an impingement of crystals before the crystallization peak maximum.

The surface nuclei density $N_s = 10^{10}\ m^{-2}$ used in this work was determined by comparing the experimental T_{imp} with the one calculated by the proposed model assuming three different values of N_s. Figure 6 shows the calculated and experimental impingement temperatures (T_{imp}) as a function of granulometry. N_s is the only fitting parameter. For stoichiometric diopside glass particles [42], N_s ranges from 10^{10} to $10^{12}\ m^{-2}$. There is a strong effect of the N_s on the calculated DSC crystallization curves, as observed in Figure 6. In the current case, $N_s = 10^{10}\ m^{-2}$, which is close to reported values of N_s for glass powders regularly prepared in laboratories, leads to the best fit between the experimental and calculated crystallization peaks. As shown in Fig. 6, by changing N_s from $10^9\ \mathrm{m}^{-2}$ to $10^{11}\ \mathrm{m}^{-2}$ the calculated impingement temperature decreased from 1220 to $1170\ °\mathrm{C}$, a difference of $50\ °\mathrm{C}$. Fig. 6 shows that the calculated values of T_{imp} are reasonably close to the experimental values, and are relatively insensitive to granulometry changes. Thus, our model properly predicts T_{imp}. In practice, however, different particles may show different N_s, but the particle ensemble may have the same average N_s. As an example, if N_s vary from $10^9\ \mathrm{m}^{-2}$ to $10^{11}\ \mathrm{m}^{-2}$ for different particles, taking particles of different size within a given granulometric range, the impingement shoulder would be smeared over a $50\ °\mathrm{C}$ temperature range.

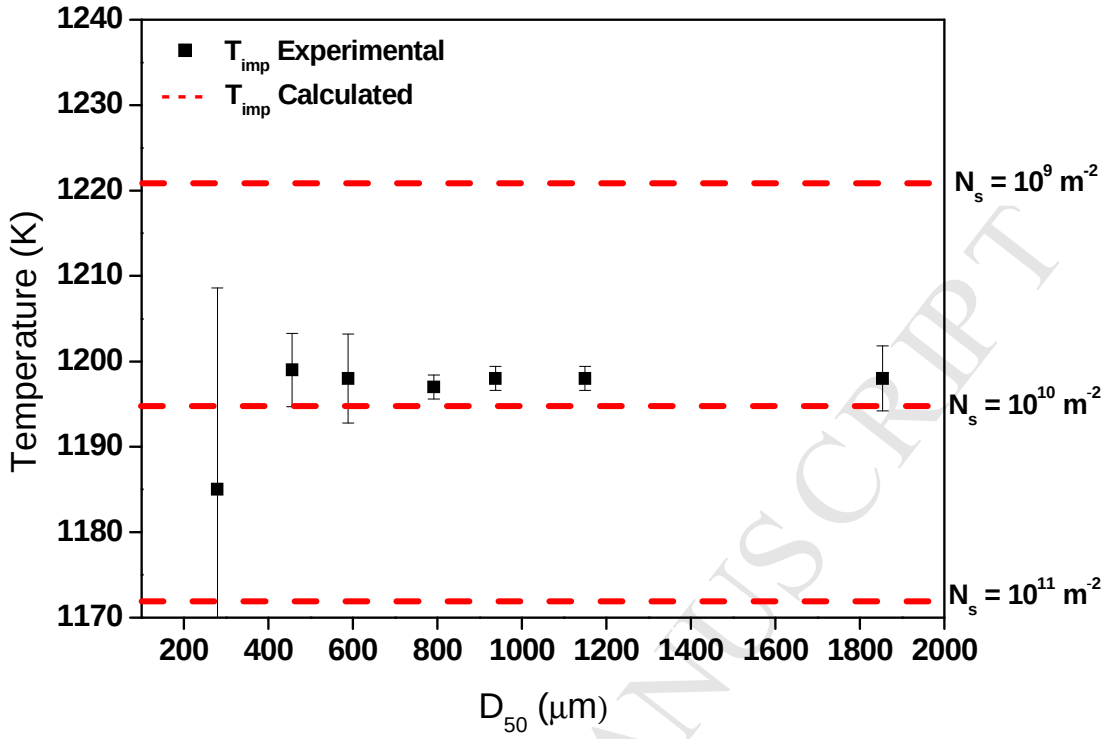

Figure 6. Experimental impingement temperature (T_{imp}) as a function of particle size. The dashed lines represent the calculated T_{imp} considering different values of surface nuclei density (N_s). The best fit is for $N_s = 10^{10}\ m^{-2}$.

5.3. Comparison between simulated and experimental diopside crystallization DSC peaks

Figure 7 shows the first experimental DSC crystallization peaks for our glass (Figure 3) compared to DSC-like crystallization curves calculated using the Eqs. (8-10) for samples with granulometry higher than 20 µm. Different simulations are shown: one using the adapted model (considering the particle size distributions of Figure 2 and the "density pores") and another using the original *Reis-Zanotto* model, using the average particle size (D_{50}) and no

pore; we also show simulations using the adapted model and a crystal growth rate equation fit to data of several authors compiled by Reinsch et al. [33]

The calculated curves reasonably agree with the experimental ones. The calculated crystallization peak maximum shifted approximately 15 K to higher temperatures for samples with particles larger than 150 µm, whereas better agreement was found for particles smaller than 150 µm.

This difference may be related to the effect of particle geometry, especially for samples larger than 50 µm. Recently, using the geometry-contraction model [30] to calculate the DSC crystallization peak of diopside glass particles of different regular shapes (cube, needle, plate, sphere, and oblate and prolate ellipsoids) and constant particle volume, some of us [30] showed that the non-isothermal crystallization kinetics determined by DSC is heavily affected by the particle shape. When the particle geometry deviates from spherical, that is, the particle geometry becomes less symmetrical, the DSC crystallization peak becomes narrower and more intense. As particles are subjected to further milling, they tend to become more symmetrical. Smaller particles are also more susceptible to rounding by viscous flow before crystallization [11]. Thus, taking into account different particle geometries seems to be an opportunity to enhance the model used in this work.

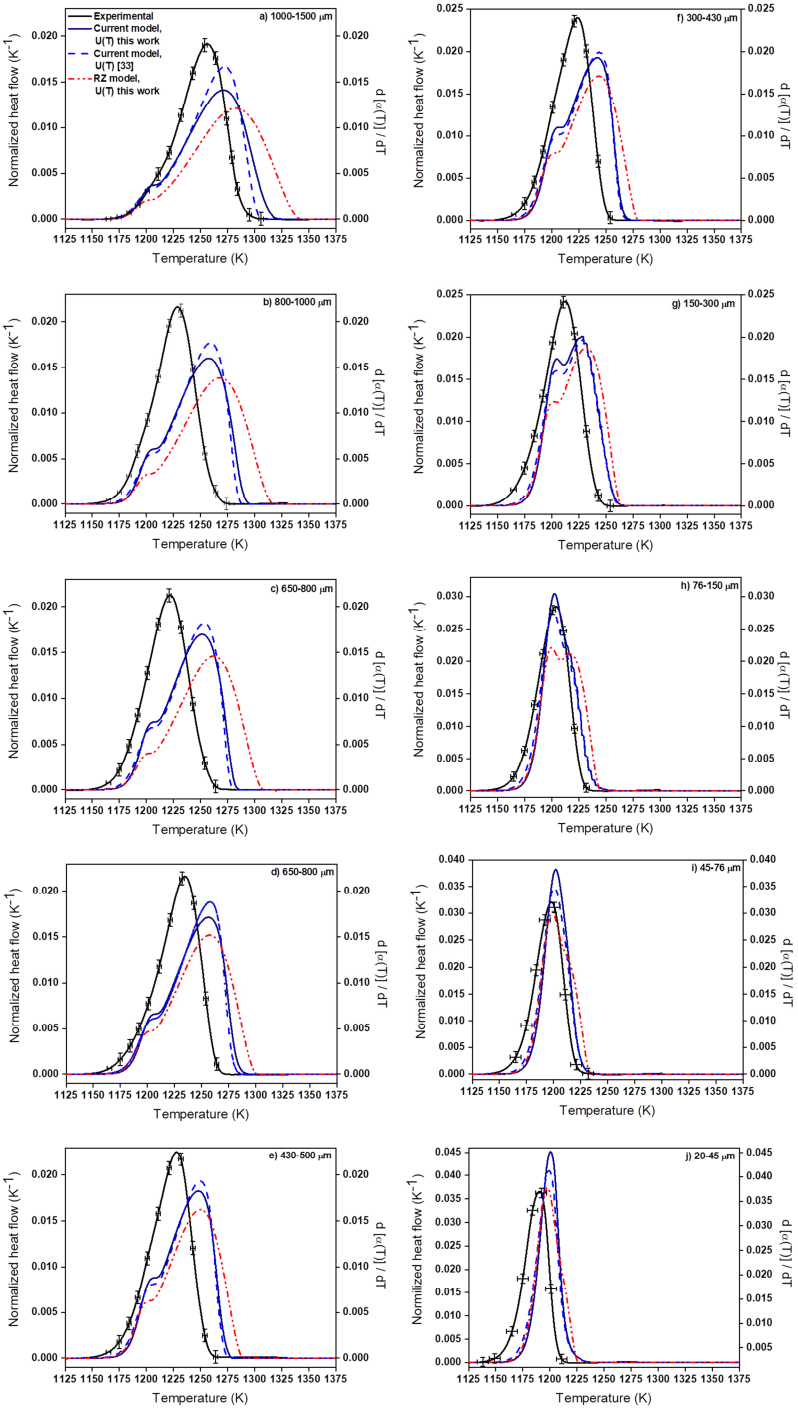

Figure 7. Experimental (LHS axes) and calculated (RHS axes) DSC crystallization curves on heating at 10 K/min for diopside glass powders with different granulometris. The curves for the original RZ model were calculated with D_{50} and $U(T)$ of this work. The curves of current revised RZ model were calculated for the indicated particle size distributions, with $U(T)$ of this work and from ref. [33]. For the calculated curves, $N_s = 10^{10}\ m^{-2}$.

In Figure 8, we compare the experimental DSC crystallization peak with the calculated one for the 500-600-µm sample, taking into account the PSD for both cases: with and without the density pore effect. For example, without density pore correction, the transformation is limited to $h^{max} = R$, i.e. the crystallization front advances down to the particle center, whereas with density pore correction, the transformation is limited to $h^{max} \cong 0.50R$. As expected, the calculated DSC crystallization peak without the density pore effect has a lower intensity and delayed crystallization end at higher temperatures than with the density correction.

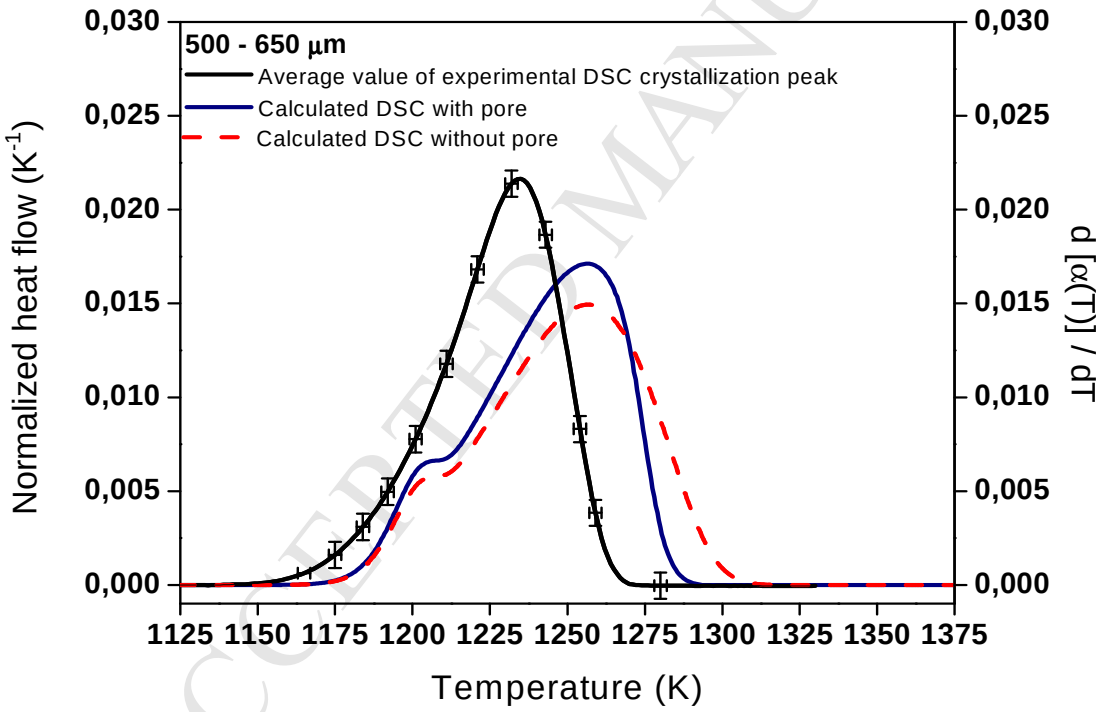

Figure 8. Experimental (LHS axis) and calculated DSC crystallization curves on heating at 10 K/min for the 500-650-µm diopside glass sample. The calculated peaks (RHS axis) were obtained with and without the effect of the crystallization-induced porosity.

Figures 7 and 8 show that when the particle size distribution and pores are taken into consideration, there is a better fit to the experimental DSC peaks than when only an average particle size is used or the pore effect is disregarded.

The use of the experimental $U(T)$ obtained for the current glass indeed makes a difference in the calculated curves and improves the agreement, however, it is not far from those calculated for diopside glasses considering $U(T)$ fitted from data of different authors. This is a fortuitous case, since the $U(T)$ data for (nominally) stoichiometric diopside glasses from different authors show a remarkable similarity, even considering that they probably have significant composition deviations and impurity levels. However, a noteworthy scatter is evident on the $U(T)$ data [33] in the temperature range between 1200 and 1300 K, the same of the DSC peaks in this work, indicating the effect of the (slightly) different glass compositions used by these authors.

It is relevant to note that the crystal growth rate on the glass surface may be different from the growth into the glass sample interior. This has been demonstrated, e.g., for combeite ($Na_2O.2CaO.3SiO_2$ or 123) glass, for which Yuritsyn et al.[43] observed that the ratio between the surface and volume crystal growth is $U_s/U_v = 1.8$ at $1.21T_g$, $U_s/U_v = 81$ at $1.07T_g$ and $U_s/U_v = 110$ at $1.03T_g$. For a diopside glass, Reis [39] noted similar values for U_s and U_v at $1.08T_g$. In our case, the first DSC crystallization peak ranges from $1.14T_g$ to $1.32T_g$ for different particle size ranges, and thus to a first approximation we expect that $U_s/U_v \cong 1$. Hence, there is no significant difference between the crystal growth on the surface and towards the volume in the temperature range of our DSC study. In our case, the crystal growth rate measured by a change of thickness of the crystallized layer (growing towards

the sample interior) as a function of time between $1.12T_g$ and $1.28T_g$ is a good approximation for both surface and volume transformation kinetics.

Finally, the RZ model extended to include the particle size and pore effect may aid in the design of the microstructure and properties of glass-ceramic materials by controlling the particle size and the sinter-crystallization path. The model could be used alongside sintering models to determine in which temperature the sample should be treated to trigger (or not) the nucleation of pores.

For example, a sintered glass-ceramic prepared from a precursor glass showing only heterogeneous nucleation, and whose crystal phase has a much higher density, could be thermally-insulating when each particle crystallizes after partial sintering until one cavitation pore forms in their center. As the rigid crystallized surface does not allow for particle shrinkage, a central pore nucleates and grows. Hence, by choosing large enough particles and a temperature above T_{imp}, a crystallized surface layer could form around each sintered particle, and this effect could maximize the trapped gas and the thermally-insulating property of the resulting glass-ceramic. On the other hand, if the same glass is prepared as fine particles, such that the number of surface nucleation sites is insufficient to form a continuous crystallized layer around each particle, it would sinter faster, and would present a crystallization behavior similar to glasses showing internal nucleation. In this case, the resulting glass-ceramic would reach a higher relative density by sinter-crystallization and would be mechanically stronger, but less thermally-insulating than in the previous case.

6. Conclusions

We adapted the *Reis-Zanotto* model for describing the crystallization kinetics of a glass particle ensemble. The revised model considers the particle size distribution and crystallization-induced porosity. These two complicating factors are quite common in practice and were not included in the original derivation of the RZ model.

We then successfully tested the modified model for a glass that shows these two features. For the largest particles, the experimental and simulated DSC peak profiles present a shoulder before the crystallization peak maximum, which was attributed to a change in the transformation dimensionality – from 3D to 1D – which occurs after impingement of the surface crystals. The temperature of the shoulder in the experimental DSC traces was consistent with $N_s = 10^{10}\ m^{-2}$ (the only fitting parameter). The very reasonable, but non-perfect, agreement between the experimental (jagged particles) and theoretical (spherical particles) peak profiles indicates that the glass particle morphology also plays a role in their non-isothermal crystallization kinetics.

The adapted model describes the complex crystallization kinetics of our glass powder, showing that the two complicating factors studied should be taken into account in future studies of glass particle crystallization.

7. Acknowledgments

The authors gratefully acknowledge the São Paulo Research Foundation (FAPESP) for funding processes 2013/07793-6 (CeRTEV) and 2013/09234-4 (Ph.D. grant), and the Coordination for the Improvement of Higher Education Personnel (CAPES) for funding the research conducted by Roger G. Fernandes during his doctoral studies.

8. References

[1] Y. Kim, S. Cang, The thermal properties of cordierite/diopside composites fabricated by glass–ceramics process for LED packages, Ceram. Int. 39 (1) (2013) S619–S622.

[2] S. A. M. Abdel-Hameed, A. A. El-kheshen, Thermal and chemical properties of diopside-wollastonite glass-ceramics in the SiO_2–CaO–MgO system from raw materials, Ceram. Int. 29 (3) (2003) 265–269.

[3] B. K. Choi, G. N. Sun, E. S. Kim, Microwave dielectric properties of diopside glass-ceramics, Ceram. Int. 39 (1) (2013) S677–S680.

[4] J. Kim, S. Hwang, W. Sung , H. Kim, Thermal and dielectric properties of glass-ceramics sintered based on diopside and anorthite composition, J. Electrocerams. 23 (2-4) (2009) 209–213.

[5] M. T. Sebastian, H. Jantunen, Low loss dielectric materials for LTCC applications: a review, Int. Mat. Rev. 53 (2) (2008) 57-90.

[6] W. M. Pogrebenkov, V.V. Shumkova, V.V. Pogrebenkova, Apatite-Diopside bioglass ceramic composites, Glass and Ceram. 61 (3-4) (2004) 87-89.

[7] I. Gutzow, R. Pascova, A. Karamanov, J. Schmelzer, The kinetics of surface induced sinter crystallization and the formation of glass-ceramic materials, J. Mat. Sci. 33 (21) (1998) 5265-5273.

[8] A. R. Studart, U. T. Gonzenbach, E. Tervoort, L. J. Gauckler, Processing routes to macroporous ceramics: a review, J. Am. Ceram. Soc. 89 (6) (2006) 1771-1789.

[9] P. Colombo, Conventional and novel processing methods for cellular ceramics, Philos. Trans. Roy. Soc. A 364 (2006) 109-124.

[10] V. O. Soares, O. Petil, E. D. Zanotto, New sintered Li_2O-Al_2O_3-SiO_2 ultra-low expansion glass-ceramic, J. Am. Ceram. Soc. 96 (4) (2013) 1143-1149.

[11] R. M. C. V. Reis, A. J. Barbosa, L. Ghussn, E. B. Ferreira, M. O. Prado, E. D. Zanotto. Sintering and rounding kinetics of irregular glass particles, J. Am. Ceram. Soc. 102 (2019) 845–854.

[12] V. M. Fokin, A. S. Abyzov, J. W. P. Schmelzer, E. D. Zanotto, Stress induced pore formation and phase selection in a crystallizing stretched glass, J. Non-Cryst. Solids 356 (2010) 1679–1688.

[13] A. S. Abyzov, J. W. P. Schmelzer, V. M. Fokin, Elastic stress in crystallization processes in finite domains, J. Non-Cryst. Solids 356 (2010) 1670-1678.

[14] R. M. C. V. Reis, E. D. Zanotto, Simple model for particle phase transformation kinetics, Acta Mater**,** 154 (2018) 228-236.

[15] W. A. Johnson, R. F. Mehl, Reaction kinetics in processes of nucleation and growth, Transactions of the AIME 135 (1939) 416-458.

[16] M. Avrami, Kinetics of phase change. I General theory, J. Chem. Phys. 7 (1939) 1103-1112.

[17] M. Avrami, Kinetics of phase change. II Transformation-time relations for random distribution of nuclei, J. Chem. Phys. 8 (1940) 212-224.

[18] M. Avrami, Granulation, phase change, and microstructure kinetics of phase change. III, J. Chem. Phys. 9 (1941) 177-184.

[19] A. N. Kolmogorov, On the statistical theory of the crystallization of metals, Bull. Acad. Sci. USSR, Math. Ser. 1 (1937) 355-359.

[20] M. C. Weinberg, D. P. Birnie III, V. A. Shneidman, Crystallization kinetics and the JMAK equation, J. Non-Cryst. Solids 219 (1997) 89-99.

[21] J. Màlek, The application of Johnson-Mehl-Avrami in the thermal analysis of the crystallization kinetics of glasses, Thermochimica Acta, 267 (1995) 61-73.

[22] E. Villa, P. R. Rios, Transformation kinetics for surface and bulk nucleation, Act. Mat. 58 (7) (2010) 2752-2768.

[23] E. B. Ferreira, M. L. F. Nascimento, H. Stoppa, E. D. Zanotto, Methods to estimate the number of surface nucleation sites on glass powders, Phys. and Chem. of Glass.: Eur. J. of Glass Sci. and Tech. Part B, 49 (2) (1998) 81-89.

[24] J Vazquez, D. G. G. Barreda, P. L. López-Alemany, P. Villares, R. Jiménez-Garay, A comparative study on the single scan and multiple scan techniques in differential scanning calorimetry: application to the crystallization of the semiconducting $Ge_{0,13}Sb_{0,23}Se_{0,64}$ alloy, Thermochem. Act. 430 (1-2) (2005) 173-182.

[25] E. B. Ferreira, V. Lopez-Richard, E. D. Zanotto, G. E. Marques, Analytical model for heterogeneous crystallization kinetics of spherical glass particles, J. Am. Ceram. Soc. 92 (11) (2009) 2616-2618.

[26] R. Müller, The influence of grain size on the overall kinetics of surface induced glass crystallization, J. Therm. Anal. 35 (3) (1989) 823-835.

[27] M. C. Weinberg, Surface nucleated transformation kinetics in 2 and 3 dimensional finite systems, J. Non-Cryst. Solids 134 (1-2) (1991) 116-122.

[28] E. Villa, P.R. Rios, Transformation kinetics for surface and bulk nucleation, Acta Mater. 58 (2010) 2752–2768.

[29] W. Jander, Reaktionen im festen Zustande bei höheren Temperaturen. Reaktionsgeschwindigkeiten endotherm verlaufender Umsetzungen, Z. Anorg. Allg. Chem., 162 (1927) 1-30.

[30] R. G. Fernandes, E. B. Ferreira, The shape of diopside glass particles probed by the non-isothermal crystallization kinetics and Differential Scanning Calorimetry, J. Non-Cryst. Solids 497 (2018) 63-70.

[31] Powder Diffraction File Inorganics Phases: alphabetical index, inorganics phases. Swarthmore, Pennsylvania: JCPDS/International Centre for Diffraction Data, 2016.

[32] R. M. C. V. Reis, V. M. Fokin, E. D. Zanotto, Determination of crystal growth rates in glasses over a temperature range using a single DSC run, J. Am. Ceram. Soc. 99 (6) (2016) 2001-2008.

[33] S. Reinsch, M. L. F. Nascimento, R. Müller, E. D. Zanotto. Crystal growth kinetics in cordierite and diopside glasses in wide temperatures ranges, J. Non-Cryst. Solids 354 (52-54) (2008) 5386-5394.

[34] L. Wondraczek, H. Behrens, Y. Tue, J. Deubener, G. W. Scherer, Relaxation and glass transition in an isostatically compressed diopside glass, J. Am. Ceram. Soc., 90 (5) (2007) 1556-1561.

[35] D. R. Cassar, Nucleation, Crystal growth, relaxation and viscous flow in Diopside and Lithium diborate glass, Ph.D. Thesis (In Portuguese), (2014).

[36] M. L. F. Nascimento, E. D. Zanotto, Does viscosity describe the kinetic barrier for crystal growth from the liquidus to the glass transition? J. Chem. Phys. 133 (17) (2010) 174701.

[37] In-Ho Jung, S. A. Decterov, A. D. Pelton, Critical thermodynamic evaluation and optimization of the CaO-MgO-SiO_2 system, J. Europ. Ceram. Soc. 25 (2005) 313-333.

[38] E. B. Ferreira, M. L. Lima, E. D. Zanotto, DSC method for determining the liquidus temperature of glass-forming systems, J. Am. Ceram. Soc., 93 [11] (2010) 3757-3763.

[39] R. M. C. V. Reis, Assessment of viscous sintering models and determination of crystal growth rate and crystallized fraction in glasses, Ph.D. Thesis (In Portuguese), (2012).

[40] M. L. F. Nascimento, Current problems in nucleation, crystal growth and diffusion in glasses, Ph.D. Thesis (In Portuguese), (2004).

[41] S. Fest, S. Reinsch, R. Müller, Milling, Sintering and Crystallization of 11BaO-25CaO-64SiO_2 Glass Powder, Inter. J. of Appl. Glass Sci. 5 (3) (2014) 236-247.

[42] R. Müller, E. D. Zanotto, V. M. Fokin, Surface crystallization of silicate glasses: nucleation sites and kinetics, J. Non-Cryst. Solids 274 (2000) 208-231.

[43] N. S. Yuritsyn, A. S. Abyzov, V. M. Fokin, Distinct crystal growth on the surface and in the interior of $Na_2O{\cdot}2CaO{\cdot}3SiO_2$ glass, J. Non-Cryst. Solids 498 (2018) 42-48.

Supplementary Materials

Table S1. Nominal and analyzed diopside glass compositions (w*t%*).

	MgO	SiO_2	CaO
Stoichiometric diopside	18.6	55.5	25.9
This work	**14.3**	**58.4**	**25.9**
Fokin et al. [12]	18.1	56.4	25.5
Cassar [35], Reis [39]	18.6	55.4	25.8
Nascimento [40]	17.9	60.1	22.0

Table S2. Sample characteristics: intercepts at 10, 50 and 90% (D_{10}, D_{50}, and D_{90}) of the cumulative size distributions, and DSC temperatures of glass transition (T_g), the onset of crystallization (T_x), impingement (T_{imp}), and peak maximum (T_p).

Sieve meshes (µm)	D_{10} (µm)	D_{50} (µm)	D_{90} (µm)	T_g (K)	T_{x1} (K)	T_{imp} (K)	T_{p1} (K)	T_{p2} (K)
< 7	4	9	19	997	1148	-	1168	-
7-20	12	24	35	997	1163	-	1183	1439
20-45	44	64	103	996	1166	-	1190	1451
45-76	70	90	129	996	1170	-	1197	1465
76-150	100	139	189	996	1171	-	1204	1464
150-300	176	280	421	996	1173	1175	1213	1459
300-430	361	457	568	996	1178	1198	1224	1461
430-500	458	589	747	996	1179	1198	1228	1459
500-650	627	792	999	996	1188	1198	1234	1464
650-800	717	938	1167	994	1187	1198	1233	1458
800-1000	880	1149	1489	994	1195	1198	1240	1458
1000-1500	1332	1854	2513	994	1204	1198	1257	1460

Table S2 presents the average T_g, $T_{x1,}$ and T_{p1}, and the corresponding 95% confidence intervals, assuming the Student t-distribution (performed in this work to represent the error bar). The average $T_g = 996\ K$ does not show any significant change as a function of particle size in the error intervals, as expected. Both the average T_{x1} and T_{p1} shift approximately 56 K and 90 K, respectively, to higher temperatures as the grain size increases. These shifts

are expected, since large particles present a low surface-to-volume ratio, and thus small numbers of surface nuclei when compared to small ones, delaying the crystallization progress. The powder packing in the DSC pan may also affect T_{x1} and T_{p1}. The characteristic temperatures of the crystallization peaks are shown in Figure S1.

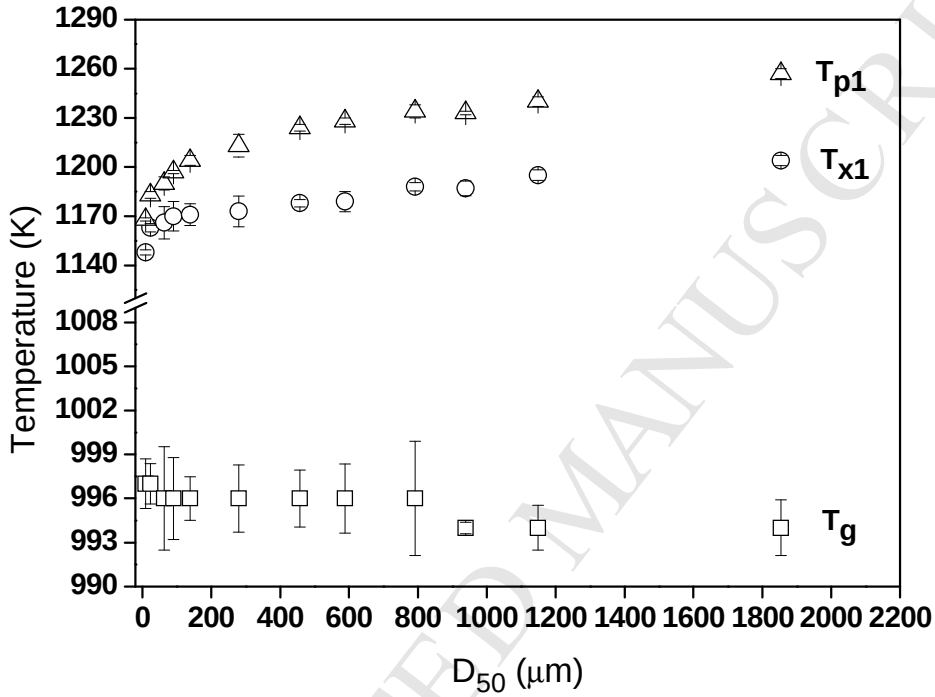

Figure S1. Characteristic temperatures of the diopside glass as a function of particle size. a) Maximum temperature (T_{p1}) and b) onset of crystallization (T_{x1}) of the first crystallization peak, and c) glass transition temperature (T_g).

Table S3. DSC heating rate (q), maximum temperature (T_{max}), the temperature of the crystallization peak 1 (T_{p1}), the temperature of the crystallization peak 2 (T_{p2}), particle shape and size from different authors for nominally stoichiometric diopside glasses.

	q (k/min)	T_{max} (K)	T_{p1} (K)	T_{p2} (K)	Shape	Size (μm)
This work	10	1763	1197	1465	Powder	45-76
This work	10	1763	1213	1459	Powder	200
Fokin et al. [12]	10	1573	1173	-	Powder	200
Reis [39]	10	1473	1184	1303	Powder	38-75
Reis *et al.* [32]	10	1473	1225	1339	Plate	130 (thickness)

Fokin *et al.* [12]	10	1573	1273	1373	monolithic	4000
Cassar [35]	9	1400	1254	1319	monolithic	-
Nascimento [40]	20	1473	1291	-	monolithic	-

Fig. 1

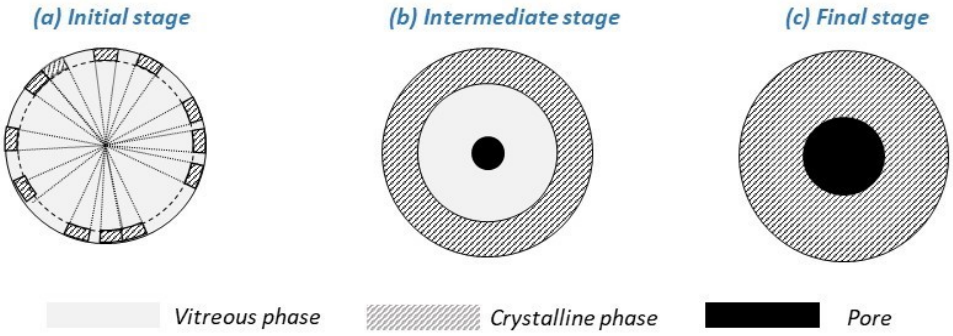

Figure 3

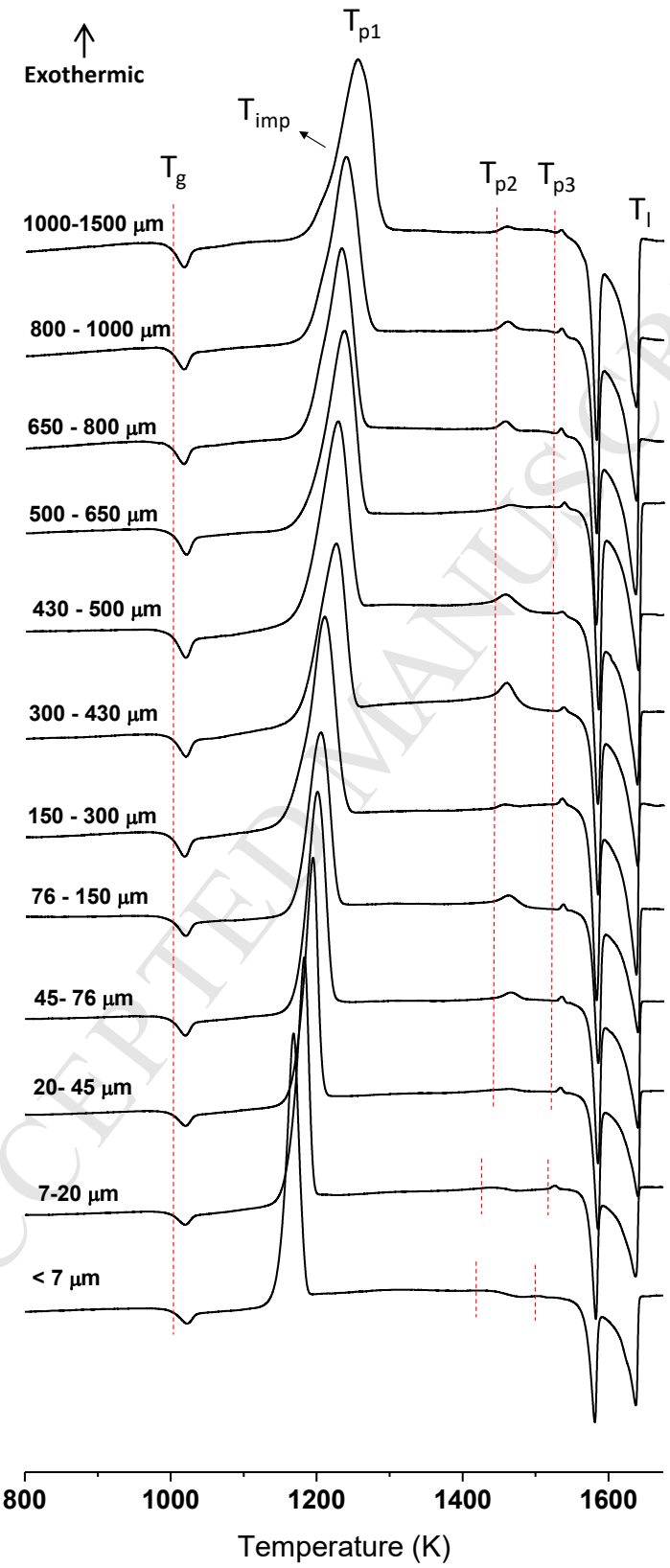

Figure 4

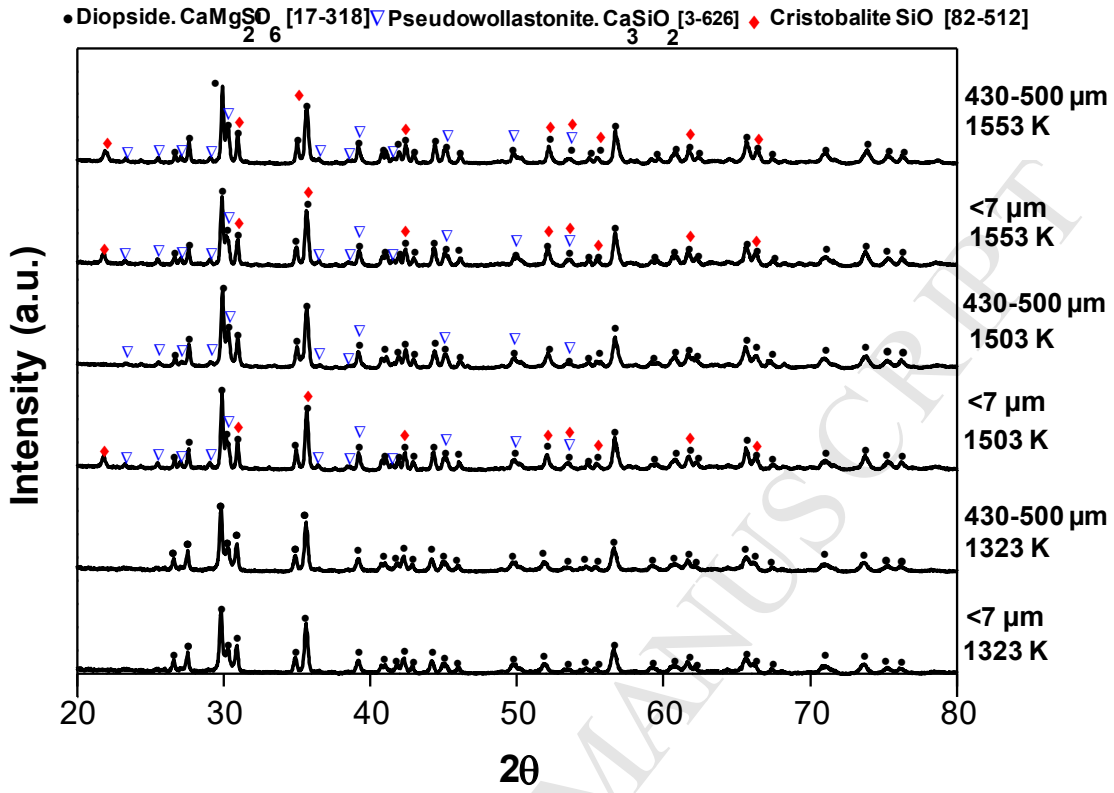

Figure 5

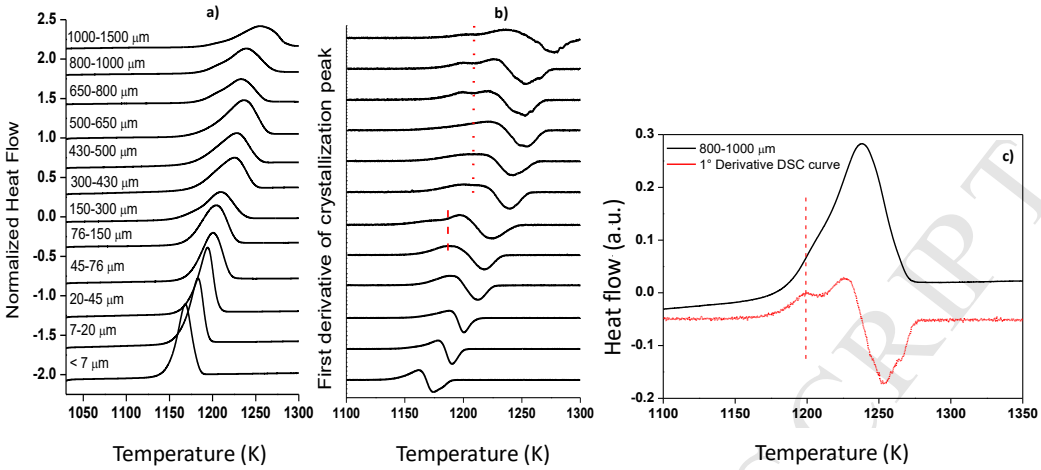

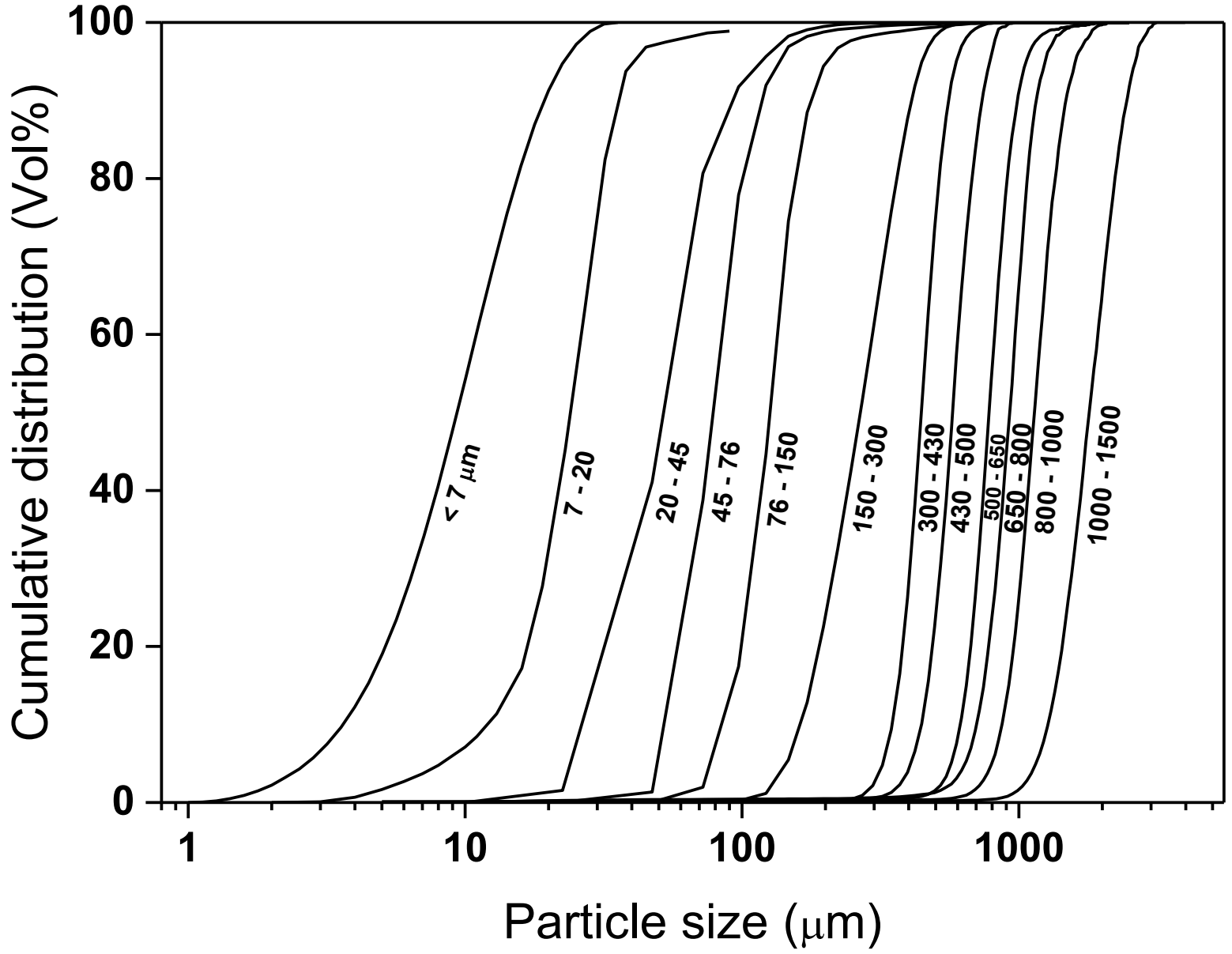
Cumulative distribution (Vol%)
100
80
60
40
20
0
1
10
100
1000
Particle size (μm)
< 7 μm
7 - 20
20 - 45
45 - 76
76 - 150
150 - 300
300 - 430
430 - 500
500 - 650
650 - 800
800 - 1000
1000 - 1500

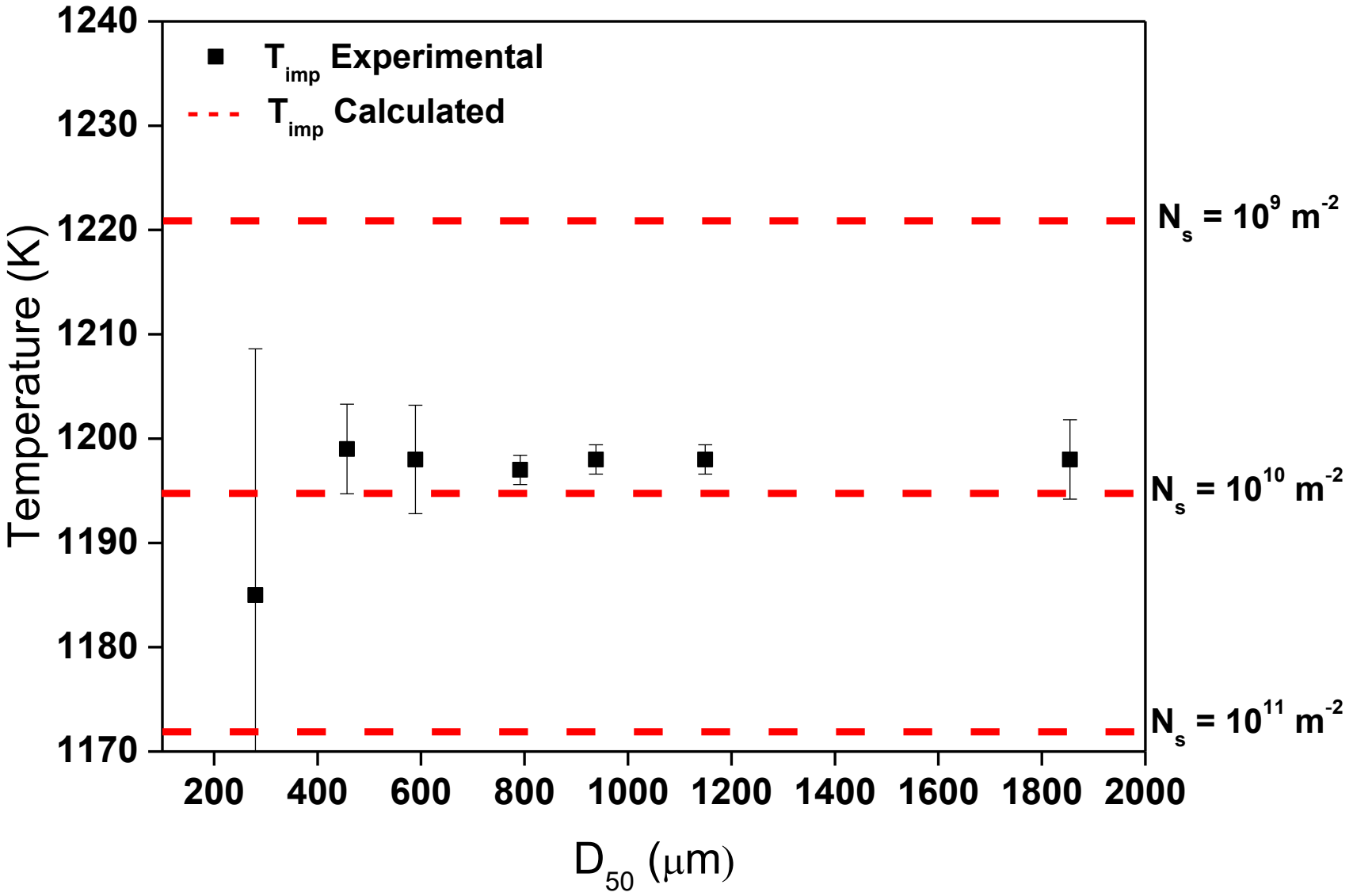
1240
1230
1220
1210
1200
1190
1180
1170
Temperature (K)
200
400
600
800
1000
1200
1400
1600
1800
2000
D50 (μm)
Timp Experimental
Timp Calculated
Ns = 10^9 m^-2
Ns = 10^10 m^-2
Ns = 10^11 m^-2

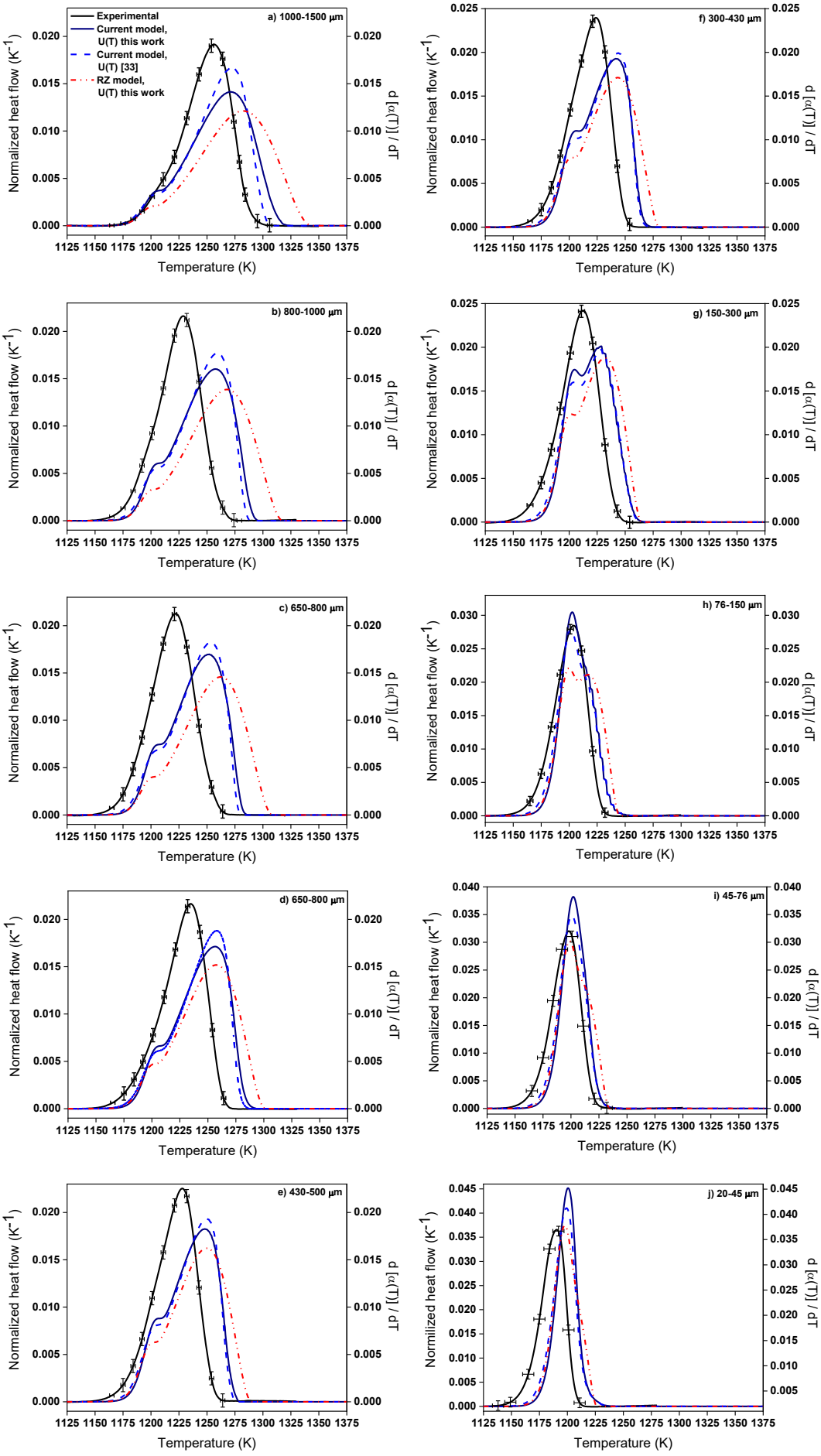
Experimental
Current model, U(T) this work
Current model, U(T) [33]
RZ model, U(T) this work
a) 1000-1500 µm
b) 800-1000 µm
c) 650-800 µm
d) 650-800 µm
e) 430-500 µm
f) 300-430 µm
g) 150-300 µm
h) 76-150 µm
i) 45-76 µm
j) 20-45 µm
Normalized heat flow (K^{-1})
d [α(T)] / dT
Temperature (K)